PHYSICAL SCIENCES

Observation of topological Hall torque exerted on a domain wall in the ferromagnetic oxide $SrRuO_3$

Michihiko Yamanouchi[1]*, Yasufumi Araki[2], Takaki Sakai[1], Tetsuya Uemura[1], Hiromichi Ohta[3], Jun'ichi Ieda[2]

In a ferromagnetic Weyl metal $SrRuO_3$, a large effective magnetic field H_{eff} exerted on a magnetic domain wall (DW) by current has been reported. We show that the ratio of H_{eff} to current density exhibits nonmonotonic temperature dependence and surpasses those of conventional spin-transfer torques and spin-orbit torques. This enhancement is described well by topological Hall torque (THT), which is exerted on a DW by Weyl electrons emerging around Weyl points when an electric field is applied across the DW. The ratio of the H_{eff} arising from the THT to current density is over one order of magnitude higher than that originating from spin-transfer torques and spin-orbit torques reported in metallic systems, showing that the THT may provide a better way for energy-efficient manipulation of magnetization in spintronics devices.

INTRODUCTION

Magnetic textures such as a domain wall (DW), created between magnetic domains with different magnetization directions, can be moved by electrical means as well as magnetic fields. One can reverse magnetization directions by shifting DWs, and thus, the DW motion driven by electrical means has attracted much attention as a writing scheme in next-generation magnetic storage devices (*1*, *2*). Two main driving mechanisms have been identified so far, i.e., spin-transfer torque (STT) (*3*–*10*) and spin-orbit torque (SOT) (*11*–*14*). The STT, which was first experimentally found in giant magnetoresistance devices (*15*), is exerted on a DW by applying a spin-polarized current to it in ferromagnets. Later, the SOT was found to be exerted on a DW by applying an in-plane current to heavy-metal/ferromagnet heterostructures, where the spin current originating from the spin Hall effect (SHE) in the heavy metal plays an important role. Since the magnitude of these torques is proportional to the spin polarization of electrons and the spin-Hall angle, respectively, highly spin-charge–coupled systems are desirable for energy-efficient DW motion. However, relatively low charge-to-spin conversion ratio is a fundamental obstacle in conventional mechanisms.

Recent developments in the topological aspects of solids may provide an essentially different route to address this issue (*16*–*18*). Magnetic order with strong spin-orbit coupling occasionally generates point-like crossing of two electronic bands, called Weyl points (WPs) (Fig. 1, A and B), which are topological objects showing two characteristics important for the enhanced DW motion (*19*, *20*). First, WPs serve as magnetic monopoles in momentum space, whose large fictitious magnetic field (the Berry curvature) is responsible for anomalous transport of electrons such as the anomalous Hall effect (AHE) in ferromagnetic metals. Second, electrons around WPs show spin-momentum locking, which is the strong correlation between electron spin and orbital motion, corresponding to the helicity structure of elementary particles. Spin-momentum locking maps electron transport to spin, which provides highly efficient charge-to-spin conversion for electrical switching of magnetization. Recent theoretical study showed that topological Hall torque (THT) is exerted on a DW by Weyl electrons emerging around WPs based on these characteristics when an electric field is applied across the DW in ferromagnets having WPs (*21*). Here, we consider the effect of Weyl electrons on DW motion as another mechanism for electrical manipulation of magnetization direction, which is the previously unidentified outcome of the topological aspects of Weyl fermions useful for spintronics application.

To scrutinize the effect, we chose $SrRuO_3$ (SRO), a metallic ferromagnetic oxide having many WPs near the Fermi level. SRO has an AHE and a spin-wave gap that show nonmonotonic temperature dependences, as explained by the Berry curvature around the WPs (*22*, *23*). Moreover, magnetotransport phenomena specific to Weyl fermions in the quantum Hall regime have been confirmed in SRO (*24*). While skyrmions, topologically nontrivial magnetic textures, by themselves lead to the topological Hall effect (THE) in SRO (*25*, *26*), the correlation of the momentum-space topology of Weyl electrons with real-space magnetic textures like DWs remains to be elucidated. An early experiment showed that a DW is efficiently moved by a current with the current density as low as 10^9 to 10^{10} A/m^2, but the mechanism is unsolved in SRO (*27*). In the previous report (*28*), we reexamined the system through modulation of coercive field for DW motion by currents revealing the large effective magnetic field H_{eff} exerted on the DW. Although the H_{eff} around the ferromagnetic transition temperature T_C seemed to be explained by the conventional field-like STT, the assumption made to explain the magnitude of H_{eff} needs to be underpinned (*28*). Here, we carry out further systematic studies in a wider temperature T range and demonstrate that the recently proposed THT (*21*) can provide the mechanism behind the large H_{eff} acting on DWs in SRO.

RESULTS AND DISCUSSION

Figure 1C is a schematic diagram of a device made of a 21-nm-thick SRO film and the measurement setup with the Cartesian coordinate system used in this study. From the magnetization measurements, the SRO film has z, y, and (a slight) x magnetization components, and T_C was estimated to be 148 K (fig. S1). The transverse resistance R_{yx} of SRO is dominated by the AHE, which reflects magnetization,

[1]Division of Electronics for Informatics, Graduate School of Information Science and Technology, Hokkaido University, Sapporo 060-0814, Japan. [2]Advanced Science Research Center, Japan Atomic Energy Agency, Tokai, Ibaraki 319-1195, Japan. [3]Research Institute for Electronic Science, Hokkaido University, N20W10, Kita-ku, Sapporo 001-0020, Japan.
*Corresponding author. Email: m-yama@ist.hokudai.ac.jp

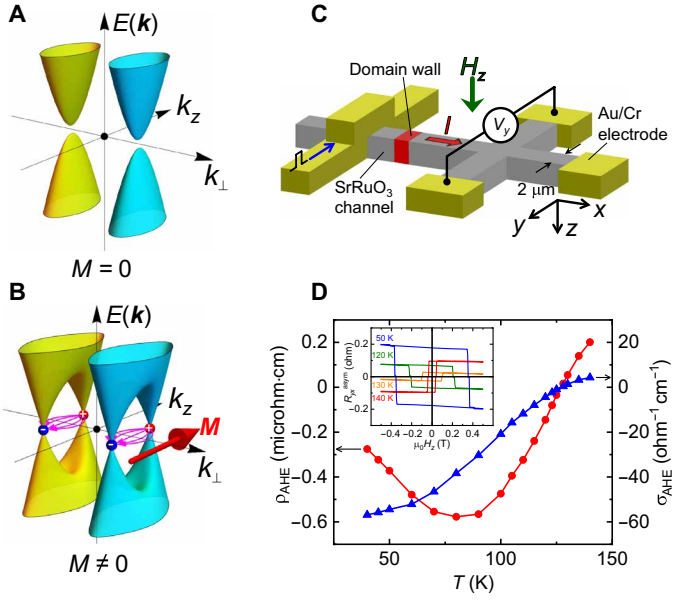

Fig. 1. Illustration of WPs, device structure, and anomalous Hall effect in $SrRuO_3$. Schematic illustrations of generation of WPs in materials with strong spin-orbit coupling for (**A**) magnetization $M = 0$ and (**B**) $M \neq 0$. (**C**) Schematic illustration of a device with a 2-μm channel, a pair of Hall probes, and a 2-μm-wide Au/Cr line (Oersted line) to generate a local Oersted field by applying a current pulse to it, and the measurement setup with the definition of the Cartesian coordinate system used in this study. (**D**) ρ_{AHE} and σ_{AHE} derived using ρ_{AHE} and ρ_{xx} as a function of T. The inset shows R_{yx}^{asym} as a function of $\mu_0 H_z$ measured at 50, 120, 130, and 140 K.

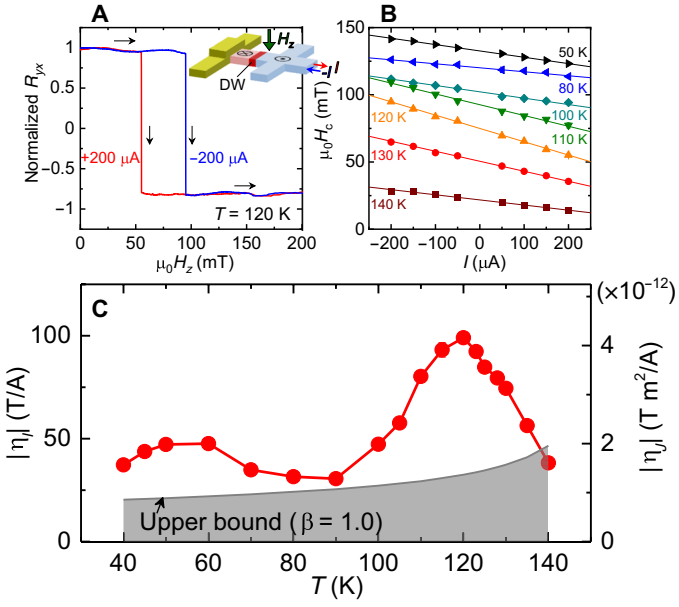

Fig. 2. Effective magnetic-field acting on domain wall by current. (**A**) Normalized R_{yx} as a function of $\mu_0 H_z$ at 120 K for $I = \pm 200$ μA after preparing a DW in the channel. The arrows show the sweep direction of $\mu_0 H_z$. The inset is a schematic illustration of DW motion under $\mu_0 H_z$ and I during the measurements. (**B**) Averaged $\mu_0 H_c$ for DW motion and SD (error bar) as a function of I determined from measurements similar to those used to make (A) at $T = 50$ to 140 K. The thin lines are linear fits to the data. (**C**) Slope η_I (magnitude) obtained from linear fits to the $\mu_0 H_c$ versus I plots measured at $T = 40$ to 140 K as a function of T shown in (B). The right-hand vertical axis in (C) is $|\eta_J|$, which is derived by converting I into current density J in $|\eta_J|$. The shaded area in (C) is within the upper bound of H_{eff} arising from the conventional field-like STT per unit current density calculated by assuming $\beta = 1$.

M_z, in the z direction and the contribution from the Berry curvature generated from the WPs. We measured R_{yx} with 20 μA while sweeping the out-of-plane magnetic field H_z, where positive (negative) H_z points in the $+z$ ($-z$) direction. The asymmetric component R_{yx}^{asym} with respect to H_z was extracted from R_{yx} to remove the contribution from the superimposed longitudinal resistance. R_{yx}^{asym} is plotted as a function of $\mu_0 H_z$ (μ_0 is the permeability of the vacuum) in the inset of Fig. 1D. Clear hysteresis indicating the existence of M_z appears at $T \leq 140$ K, which enables the magnetization reversal around the Hall probes to be investigated by monitoring R_{yx}. Figure 1D shows the anomalous Hall resistivity ρ_{AHE} derived from R_{yx}^{asym} at $\mu_0 H_z = 0$ swept back from +0.5 T and the anomalous Hall conductivity σ_{AHE} derived from ρ_{AHE} and the longitudinal conductivity ρ_{xx} as a function of T. ρ_{AHE} exhibits a nonmonotonic T dependence and changes its sign from negative to positive with increasing T, whereas M_z monotonically decreases with increasing T (fig. S1). These results indicate the critical role of the Berry curvature on the AHE in the present SRO film (*22*). The in-plane magnetic-field angle dependence of R_{yx} (fig. S2) and the magnetization measurements (fig. S1) indicate that the uniaxial magnetic easy axis, whose tilting angle from the film normal varies with temperature, and the in-plane component dominantly points in the y direction. This magnetic anisotropy field stabilizes the Bloch wall in the channel of the present device.

We evaluated the modulation of the coercive field H_c for the DW motion by current I to determine the effective magnetic field H_{eff} acting on a DW. Figure 2A plots the normalized R_{yx} as a function of $\mu_0 H_z$ at 120 K under $I = \pm 200$ μA after preparing a DW in the channel, where positive (negative) I is defined as a current in the $+x$ ($-x$) direction. The same measurement was repeated three times, and the values of H_c were averaged. We carried out similar measurements under $|I| \leq 200$ μA at various temperatures, where the temperature increase by Joule heating was determined from the variation in the longitudinal resistance to be less than 0.4 K in the measured current range. The averaged H_c and SD (error bar) at $T = 50$ to 140 K are plotted as a function of I in Fig. 2B, where the error bars are smaller than the size of symbols. H_c linearly decreases with increasing I, which indicates that I acts as an H_{eff} in the z direction on the DW and moves it in the I direction, as reported previously (*27*, *28*). We fitted a line to the data in Fig. 2B to obtain the slope η_I, which corresponds to the ratio of $\mu_0 H_{eff}$ to I. The value of η_I determined from similar measurements made at various Is and Ts is summarized in Fig. 2C. The slope with respect to the current density J, denoted as η_J, is also shown in Fig. 2C. The absolute value of η_I ($|\eta_J|$) exhibits a nonmonotonic T dependence, whereas total magnetization gradually decreases with increasing T (fig. S1). These results indicate that variations in the total magnetization cannot fully explain the T dependence of H_{eff}.

Let us examine the conventional STT and SOT mechanisms as possible explanations for the H_{eff} observed in SRO considering our previous study (*28*). The first is an H_{eff} induced by the field-like STT originating from spin relaxation of conduction electrons in the DW (*9*, *10*). This H_{eff} drives the DW in the current direction in SRO with a negative transport spin polarization (*29*), and it is consistent with the observation. We estimated an upper bound of $\mu_0 H_{eff}/J$ by assuming a dimensionless nonadiabaticity parameter, $\beta = 1$, which is usually less than unity, and that parameters other than the magnetization are T independent (see Materials and Methods and Table 1).

The value of $\mu_0 H_{eff}/J$ induced by the field-like STT is within the shaded area in Fig. 2C because reduction of the transport spin polarization and increase of the DW width with increasing T are neglected. The observed η_J is beyond the upper bound except near T_C, and hence, the field-like STT cannot fully account for the observed H_{eff}. The second is an out-of-plane H_{eff} resulting from the Slonczewski-like SOT exerted on chiral DWs, as has been reported for heavy-metal/ferromagnet heterostructures (*12*, *13*). Although the present structure consists of a single layer, the SHE, which plays a critical role in the Slonczewski-like SOT, has been reported even at a temperature below T_C in SRO (*30*). Supposing that a chiral DW is formed and the reported spin Hall angle is used (*30*), $\mu_0 H_{eff}/J$ at 50 K is calculated to be 2.7×10^{-14} T m^2/A, which is two orders of magnitude less than the observed values, and hence negligible (Materials and Methods and Table 1). The third is an in-plane H_{eff} (in the y direction) caused by field-like SOT (*31*). This H_{eff} acts on magnetization in the y direction and modulates H_c in the opposite sense depending on the magnetization configuration. We confirmed that, on the contrary, the direction of the current-induced DW motion was independent of the magnetization configuration in a similar SRO device (fig. S3), which rules out the field-like SOT.

Now, let us consider the impact of the nontrivial momentum ($\boldsymbol{k}$)-space topology of the Weyl electrons on the unconventional torque observed in SRO (*21*). Under spin-momentum locking with the tensor structure $\boldsymbol{\Lambda_k}$, an electron moving at velocity $\boldsymbol{V_k}$ shows a spin polarization $\sigma = \boldsymbol{\Lambda_k}^{-1}\boldsymbol{V_k}$. Therefore, the local spin density contributing to the torque on a DW is given in the semiclassical formalism (*32*) as

$$\langle \sigma \rangle = \int d^3\boldsymbol{k}/(2\pi)^3 F_{\boldsymbol{k}} \boldsymbol{\Lambda_k}^{-1} \boldsymbol{V_k} \quad (1)$$

where $F_{\boldsymbol{k}}$ represents the $\boldsymbol{k}$-space distribution of electrons around the DW. From the Berry curvature of Weyl electrons, an electric field $\boldsymbol{E}$ drives the anomalous velocity $\boldsymbol{V_k^A} \| \boldsymbol{M} \times \boldsymbol{E}$, where $\boldsymbol{M}$ denotes the magnetization vector, resulting in the AHE. This $\boldsymbol{V_k^A}$, which is transverse to $\boldsymbol{E}$, generates a finite $\langle \boldsymbol{\sigma} \rangle$ via Eq. 1 once the inversion symmetry of $F_{\boldsymbol{k}}$ is broken by a DW. Notably, the emergence of this spin polarization is independent of the transport relaxation time and thus robust under disorder (*21*), which is sharply distinct from the angular momentum transfer carried by the spin current. Since this contribution requires nontrivial topologies in both real space (DWs) and $\boldsymbol{k}$-space (WPs) and stems from the transverse (Hall) component of $\boldsymbol{V_k}$, we call the resulting torque THT.

As a prominent feature, THT is enhanced near the WPs where both the Berry curvature and the spin-momentum locking become notable. To show this, we performed a model calculation using a minimal two-band system, as shown in Fig. 3 (A to D) (see Materials and Methods). This model consists of two pairs of WPs near the

Table 1. $\mu_0 H_{eff}/J$, the ratio of current-induced effective magnetic-field acting on a DW to current density, in typical ferromagnetic metal systems and $SrRuO_3$. Experimental values for permalloy (*5*), Co/Pt bilayer (*7*), Ta/CoFeB/MgO trilayer (*13*), and $SrRuO_3$ (this work) are listed together with the underlying mechanism (field-like STT, Slonczewski-like SOT, or THT). Theoretically calculated estimates based on each mechanism are presented for $SrRuO_3$.

	Permalloy	Co/Pt	Ta/CoFeB/MgO	$SrRuO_3$		
$\mu_0 H_{eff}/J$ (Tm^2/A)	~10^{-15} (*5*)	~5×10^{-14} (*7*)	1.7×10^{-13} (*13*)	1.3×10^{-12} to 4.2×10^{-12} (this work)		
Calc.	–	–	–	$<2 \times 10^{-12}$	2.7×10^{-14}	$>10^{-12}$
Mechanism	Field-like STT	Field-like STT	Slonczewski-like SOT	Field-like STT	Slonczewski-like SOT	THT

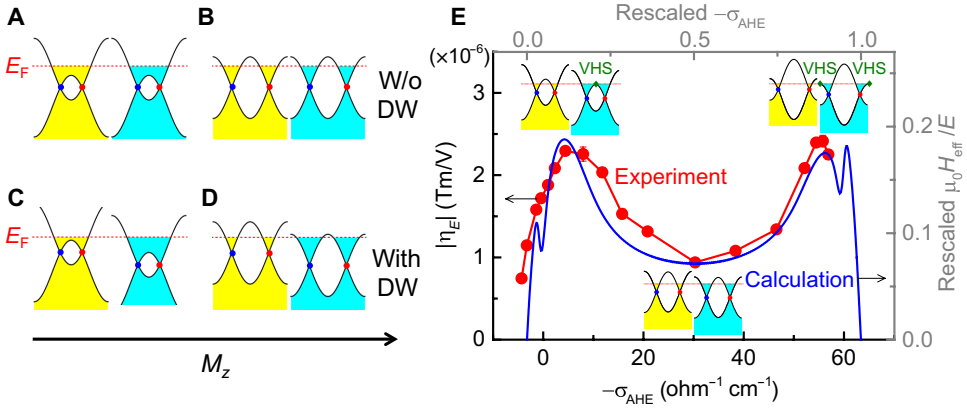

Fig. 3. Two-band model having two pairs of WPs and comparison of observed and calculated topological Hall torque based on the model. Schematic images of variation in the two bands for cases (**A** and **B**) without and (**C** and **D**) with a DW, with respect to M_z. For the DW case, the two bands shift in opposite directions with respect to the Fermi level E_F by varying M_z, due to the breaking of inversion symmetry by the DW. (**E**) Magnitude of ratio of $\mu_0 H_c$ to electric field E applied to the channel as a function of sign-reversed anomalous Hall conductivity $-\sigma_{AHE}$, which was derived by converting J into E and T into $-\sigma_{AHE}$ at each temperature in the $|\eta_J|$ versus T plot shown in Fig. 2C. The rescaled $|\mu_0 H_{eff}/E|$ as a function of rescaled $-\sigma_{AHE}$ calculated from Eq. 2 is also shown. The insets are schematic images of the two bands corresponding to the peaks and dip. The peaks arise from the van Hove singularity (VHS).

Fermi level, which are related by inversion symmetry. The monotonic behavior in σ_{AHE} with respect to temperature, or magnetization, is consistently described by this minimal model without incorporating the other nodal structures away from the Fermi level. By applying Eq. 1 to our model Hamiltonian, the THT contribution to H_{eff} on the DW is given by

$$\mu_0 \boldsymbol{H}_{\mathrm{eff}} = -\Gamma_{\mathrm{ex}} e(\boldsymbol{E}\cdot\nabla)\boldsymbol{M}\int \frac{d^3\boldsymbol{k}}{(2\pi)^3}\frac{f'(\epsilon_{\boldsymbol{k}})}{c_{\mathrm{F}}^2}\epsilon_{\boldsymbol{k}}\left(\Omega_{\boldsymbol{k}}^{\parallel}\right)^2 \quad (2)$$

Here, Γ_{ex} is the coupling constant for the exchange coupling $-\Gamma_{ex}\boldsymbol{M}\cdot\sigma$, e is the elementary charge, $f'(\epsilon_{\boldsymbol{k}})$ is the derivative of the Fermi distribution function, $\epsilon_{\boldsymbol{k}}$ is the band energy of electrons, c_F is the Fermi velocity around the WPs, and $\Omega_{\boldsymbol{k}}^{\parallel}$ is the $\boldsymbol{k}$-space Berry curvature along the direction of $\boldsymbol{M}$ (see Materials and Methods for the derivation). The structure of the THT here is formally compatible with the field-like STT, although its origin is not the transport spin current flowing through the DW. By inserting the values typical in SRO, we estimate the magnitude of $\mu_0 H_{eff}/J$ to be 10^{-12} Tm^2/A, which formally corresponds to the nonadiabaticity parameter $\beta_{THT} \approx 2$ and matches the measured value (see Materials and Methods and Table 1).

To confirm the above scenario, we replotted the data shown in Fig. 2C as a function of $-\sigma_{AHE}$ derived at each T with converting J into the strength of the electric field E applied to the channel. Figure 3E shows the replotted $|\eta_E|$ from Fig. 2C and the corresponding $|\mu_0 H_{eff}/E|$ calculated from Eq. 2 and rescaled by constant values. The nonmonotonic behavior of $|\eta_E|$ is well reproduced: The peak in $|\eta_E|$ can be attributed to the van Hove singularity in the density of states and the strong Berry curvature between the WPs near the Fermi level, both of which become notable around σ_{AHE}~0 or the saturation value corresponding to the pair-creation/annihilation of WPs (Fig. 3E, inset). These nontrivial correspondences strongly support the proposed scenario in which the THT critically contributes to the enhancement in the observed H_{eff}, and thus, it offers an energy-efficient scheme for electrical manipulation of the magnetization direction.

The present study indicates that a ferromagnet having WPs near the Fermi level experiences an unconventionally large H_{eff} that drives the DWs. The ratio of $\mu_0 H_{eff}$ to J surpasses those of conventional STTs and SOTs and exhibits a T-dependent enhancement. These characteristic features are well described by THT, an effect that is induced by spin polarization due to the anomalous velocity from the Berry curvature and spin-momentum locking of Weyl fermions under inversion symmetry breaking by the DW. The present results prove that topological physics greatly enriches the options for energy-efficient manipulation of magnetism and is prospective for applications.

MATERIALS AND METHODS

Sample fabrication

Twenty-one–nanometer–thick SRO films were grown on a (001) $SrTiO_3$ substrate with about a 2° miscut along [100] by pulsed laser deposition using a KrF excimer laser (λ = 248 nm). The miscut substrates were used to orient the in-plane component of the uniaxial magnetic easy axis to the y direction (parallel to the miscut direction). During growth, the substrate temperature and oxygen pressure were kept at 550°C and 10 Pa, respectively. X-ray 2θ/θ diffraction scans on the fabricated films revealed diffraction peaks only from the film and substrate, and the peak from the film was consistent with that from (110) orthorhombic SRO grown on (001) $SrTiO_3$ substrate. One of the films, which was studied in our previous experiments on current-induced DW motion (*28*), was processed into Hall bar devices with a 2-μm-wide channel and a pair of Hall probes by conventional photolithography and Ar ion milling, where its channel direction (x direction) was perpendicular to the miscut direction (y direction). From the miscut direction, [001] and [$\bar{1}$10] of SRO film are predominantly directed to the x and y axes (*33*). After that, electrodes and a 2-μm-wide line (Oersted line) along the y axis were defined on the channel by lift-off of Au/Cr (Fig. 1C). The Oersted line was used to prepare a DW around it by generating a local Oersted field.

Measurement for modulation of H_c by current

After the magnetization direction in the channel was aligned by $\mu_0 H_z$ = −0.5 T, a DW was prepared in the vicinity of the Oersted line by applying a current pulse (32 to 56 mA) with the duration of 100 μs to it with the assistance of a small positive $\mu_0 H_z$ (3 to 110 mT). Then, R_{yx} was measured by applying a dc current I to the channel while sweeping H_z in the $+z$ direction to move the DW in the $+x$ direction. H_c was defined as the magnetic field giving a normalized R_{yx} of 0. The same measurement was repeated three times at each current. The averaged H_c and SD (error bar) are shown as a function of I in Fig. 2B, where the error bars are smaller than the size of symbols.

Estimation of the upper bound for the field-like STT

The ratio $\mu_0 H_{eff}/J$ for the field-like STT is expressed as $\mu_0 H_{eff}/J = \mu_0\beta\pi\hbar P_s/2\delta_w eM$, where β, $\hbar$, P_s, δ_w, e, and M are a dimensionless parameter characterizing nonadiabaticity, the reduced Planck constant, the transport spin polarization, the DW width, the elementary charge, and the magnetization, respectively (*10*). We estimated an upper bound of $\mu_0 H_{eff}/J$ by assuming that β, which usually takes a value smaller than 1 (*9*, *10*), is equal to β = 1, and parameters other than M are independent of T for simplicity. $\mu_0 H_{eff}/J$ was calculated by substituting δ_w ~ 3 nm (*34*), $|P_s| \approx 0.5$ (*35*) obtained at low temperature, and M obtained from the magnetization measurements into the expression and considering the tilting of the magnetization from the film normal.

Estimation of the Slonczewski-like SOT

The ratio $\mu_0 H_{eff}/J$ for the Sloczewski-like SOT acting on the DW is expressed as $\mu_0 H_{eff}/J = \pi\mu_0\theta_{SH}^{eff}\hbar/4eMt$, where θ_{SH}^{eff} and t are the effective spin Hall angle for the SRO layer and thickness of the SRO layer, respectively (*12*). Assuming that a chiral DW is formed in the present SRO and substituting the reported θ_{SH}^{eff} of ~0.25 at 50 K (*30*) into this expression, $\mu_0 H_{eff}/J$ is calculated to be 2.7 × 10^{-14} T m^2/A, which is two orders of magnitude less than the observed values.

The THT contribution from the WPs

To estimate the THT contribution from the WPs of SRO, we used a two-band model $H_{\boldsymbol{k}} = \boldsymbol{h}_{\boldsymbol{k}}\cdot\sigma$ that holds two pairs of WPs, as shown in Fig. 1B, to satisfy inversion symmetry, $\boldsymbol{h}_{\boldsymbol{k}} = \boldsymbol{h}_{-\boldsymbol{k}}$, and spin-momentum locking for the uniformly magnetized SRO (*21*). A van Hove singularity point appears in the middle of two WPs. The paired WPs are separated along the direction of $\boldsymbol{M}$, which we take here as the z axis. The WPs are configured to reproduce σ_{AHE} in the xy plane. When

$|\sigma_{AHE}|$ rises from zero with decreasing T, WPs are pair created and then move away from one another, as schematically shown in Fig. 3 (A and B). Around each pair of points, we impose a spin-momentum locking structure characterized by the tensor $\boldsymbol{\Lambda}_{\boldsymbol{k}} = \nabla_k \boldsymbol{h}_{\boldsymbol{k}}$, which is odd under inversion of $\boldsymbol{k}$. On the basis of the cubic symmetry of the crystal, we set an isotropic structure $\Lambda_{xx} = \Lambda_{yy} = c_{\boldsymbol{k}}$ and the off-diagonal components to zero, with $c_{\boldsymbol{k}} = +c_F$ for one pair of WPs and $c_{\boldsymbol{k}} = -c_F$ for its inversion partner.

When inversion symmetry is broken by a DW, the energies of the inversion partners are shifted as shown in Fig. 3 (C and D). This energy shift can be evaluated by regarding the magnetic texture as the effective gauge field for the Weyl fermions on the basis of spin-momentum locking (*36*, *37*). At the DW, this effective gauge field yields an effective magnetic field $\boldsymbol{b}_{\boldsymbol{k}} = (\Gamma_{ex}/ec_{\boldsymbol{k}})(\nabla \times \boldsymbol{M})$. This $\boldsymbol{b}_{\boldsymbol{k}}$ acts on the orbital part of the Weyl fermions and leads to the energy shift $\Delta\epsilon_{\boldsymbol{k}} = -\mu_{\boldsymbol{k}} \cdot \boldsymbol{b}_{\boldsymbol{k}}$, where $\boldsymbol{\mu}_{\boldsymbol{k}} = e\epsilon_{\boldsymbol{k}}\boldsymbol{\Omega}_{\boldsymbol{k}}$ is the orbital magnetic moment of a wave packet of a Weyl fermion. Therefore, at first order in the magnetic texture, the shift is given as $\Delta\epsilon_{\boldsymbol{k}} = -(\Gamma_{ex}/c_{\boldsymbol{k}})\epsilon_{\boldsymbol{k}}\Omega_{\boldsymbol{k}} \cdot (\nabla \times \boldsymbol{M})$ for the effective model defined above, which yields a correction to the distribution function $\Delta F_{\boldsymbol{k}} = f'(\epsilon_{\boldsymbol{k}})\,\Delta\epsilon_{\boldsymbol{k}}$. Since $c_{\boldsymbol{k}}$ is odd in $\boldsymbol{k}$, $\Delta\epsilon_{\boldsymbol{k}}$ under the DW generates an energy imbalance between the two pairs of WPs. In particular, if the Fermi level is in the vicinity of the van Hove singularity (see the insets of Fig. 3E), the DW-induced energy shift leads to a large $\Delta F_{\boldsymbol{k}}$. The applied electric field $\boldsymbol{E}$ gives rise to an anomalous velocity $\boldsymbol{V}^A_{\boldsymbol{k}} = e\boldsymbol{E} \times \boldsymbol{\Omega}_{\boldsymbol{k}}$. By substituting these values of $\Delta F_{\boldsymbol{k}}$ and $\boldsymbol{V}^A_{\boldsymbol{k}}$ in Eq. 2, we obtain Eq. 2 for the effective field $\mu_0\boldsymbol{H}_{eff} = \Gamma_{ex}\langle\boldsymbol{\sigma}\rangle$ of the magnetic texture, which we identify as the THT contribution.

Direction of the H_{eff} induced by the THT directly reflects the sign of $\epsilon_{\boldsymbol{k}}$ and also depends on the polarity of the DW, i.e., $\partial_x\boldsymbol{M}$. For instance, when the Fermi level locates at the upper band beyond the WPs ($\epsilon_{\boldsymbol{k}} > 0$), the current-induced DW motion is induced along the current-flowing direction irrespective of the up-down and down-up DWs as observed in the present study using SRO. In addition, the chirality of the DW that changes the direction of the Berry curvature inside the DW does not alter the direction of the H_{eff} since it contributes to the THT in a squared form of the Berry curvature $(\Omega^{\parallel}_{\boldsymbol{k}})^2$ via the anomalous velocity and the shift of electron distribution function simultaneously. The temperature dependence of the generation efficiency $|\mu_0 H_{eff}/E|$ of the THT origin comes from the Fermi distribution function as well as from the reorientation of the WPs near the Fermi level associated with the temperature dependence of the magnetization $\boldsymbol{M}$, which is a unique band character of the Weyl fermions significantly affecting on the distribution of the Berry curvature.

Estimation of the THT by model calculation

On the basis of Eq. 2, the THT contribution to H_{eff} is evaluated numerically by using the two-band model of Weyl fermions defined on a hypothetical cubic lattice (*21*). The momentum-space integral is performed on the mesh of 200 × 200 × 320 points in the cubic Brillouin zone. The Fermi level is fixed throughout the calculation, at the energy $E_F \sim 1/10$, the bandwidth beyond the WPs. We also fix the temperature in the distribution function $f(\varepsilon)$, namely, the broadening of the Fermi distribution, to the fixed value (~half of E_F) and evaluate the temperature dependence only via the magnetization $\boldsymbol{M}$. By considering the lattice spacing a in the momentum integral in Eq. 2, the lattice calculation value of H_{eff} scales with the system parameters as

$$\frac{\mu_0 H_{eff}}{E} = Z_{lat} \times \frac{\mu_0 \pi\hbar\,\Gamma_{ex}^2 ea}{M\delta_w c_F^2}$$

where $Z_{lat} = a^{-1}(2\pi)^{-3}\int d^3\boldsymbol{k} f'(\epsilon_{\boldsymbol{k}})\,\epsilon_{\boldsymbol{k}}(\Omega^{\parallel}_{\boldsymbol{k}})^2$ is the dimensionless quantity determined by the band structure around the WPs. By the numerical integration with the lattice model, we find that $Z_{lat} \lesssim 0.2$. By comparing this form of H_{eff} with the field-like STT, $\mu_0 H_{eff}/J = \mu_0\beta\pi\hbar P_s/2\delta_w eM$, we find that the efficiency of the THT is compatible with the field-like STT with the nonadiabaticity parameter $\beta_{THT} = 2Z_{lat}a\Gamma_{ex}^2 e^2\rho/c_F^2 P_s$.

By inserting the following values into the above relation, $M \sim 0.2$ T, $\rho_{xx} \sim 100$ microhm·cm, DW width $\delta_w \sim 3$ nm (*34*), $\Gamma_{ex}M \sim 0.6$ eV, $a \sim 4$ Å obtained from first-principles calculations (*38*), and $c_F \sim 1$ eVÅ, which is a typical value of c_F in Weyl semimetals, we estimate the magnitude of $\mu_0 H_{eff}/J$ to be $\sim 10^{-12}$ Tm^2/A and the nonadiabaticity parameter $\beta_{THT} \sim 2$, which matches the measured value.

We also investigate the numerical behavior of $|\mu_0\boldsymbol{H}_{eff}|$ from the THT with respect to σ_{AHE}. When we compare the calculated σ_{AHE} and H_{eff} with the measured values, we note that there may be multiple WPs (more than four in our model) contributing to those quantities. Moreover, the metallic bands apart from the WPs necessarily give additive contributions to them. Although those effects may depend the details of band structure, here we take them into account in our calculation phenomenologically by shifting σ_{AHE} by a constant value and multiplying constant factors on σ_{AHE} and H_{eff}. By choosing those rescaling parameters properly, we are successful in reproducing the measured peak and dip structures in $|\mu_0 H_{eff}/E|$ with respect to σ_{AHE} in Fig. 3E.

SUPPLEMENTARY MATERIALS

Supplementary material for this article is available at https://science.org/doi/10.1126/sciadv.abl6192

REFERENCES AND NOTES

1. S. S. P. Parkin, S.-H. Yang, Memory on the racetrack. *Nat. Nanotech.* **10**, 195–198 (2015).
2. S. Fukami, T. Suzuki, K. Nagahara, N. Ohshima, Y. Ozaki, S. Saito, R. Nebashi, N. Sakimura, H. Honjo, K. Mori, C. Igarashi, S. Miura, N. Ishiwata, T. Sugibayashi, Low-current perpendicular domain wall motion cell for scalable high-speed MRAM. *Digest Tech. Pap.*, 230–231 (2009).
3. A. Yamaguchi, T. Ono, S. Nasu, K. Miyake, K. Mibu, T. Shinjo, Real-space observation of current-driven domain wall motion in submicron magnetic wires. *Phys. Rev. Lett.* **92**, 077205 (2004).
4. M. Yamanouchi, D. Chiba, F. Matsukura, H. Ohno, Current-induced domain-wall switching in a ferromagnetic semiconductor structure. *Nature* **428**, 539–542 (2004).
5. M. Hayashi, L. Thomas, Y. B. Bazaliy, C. Rettner, R. Moriya, X. Jiang, S. S. P. Parkin, Influence of current on field-driven domain wall motion in permalloy nanowires from time resolved measurements of anisotropic magnetoresistance. *Phys. Rev. Lett.* **96**, 197207 (2006).
6. O. Boulle, J. Kimling, P. Warnicke, M. Kläui, U. Rüdiger, Nonadiabatic spin transfer torque in high anisotropy magnetic nanowires with narrow domain walls. *Phys. Rev. Lett.* **101**, 216601 (2008).
7. J. H. Franken, M. Herps, H. J. M. Swagten, B. Koopmans, Tunable chiral spin texture in magnetic domain-walls. *Sci. Rep.* **4**, 5248 (2014).
8. G. Tatara, H. Kohno, J. Shibata, Theory of domain wall dynamics under current. *J. Phys. Soc. Jpn.* **77**, 031003 (2008).
9. S. Zhang, Z. Li, Roles of nonequilibrium conduction electrons on the magnetization dynamics of ferromagnets. *Phys. Rev. Lett.* **93**, 127204 (2004).
10. A. Thiaville, Y. Nakatani, J. Miltat, Y. Suzuki, Micromagnetic understanding of current-driven domain wall motion in patterned nanowires. *Eur. phys. Lett.* **69**, 990–996 (2005).
11. L. Liu, C. Pai, Y. Li, H. M. Tseng, D. C. Ralph, R. A. Buhrman, Spin-torque switching with the giant spin hall effect of tantalum. *Science* **336**, 555–558 (2012).
12. A. Thiaville, S. Rohart, É. Jué, V. Cros, A. Fert, Dynamics of Dzyaloshinskii domain walls in ultrathin magnetic films. *Eur. Phys. Lett.* **100**, 57002 (2012).
13. S. Emori, U. Bauer, S.-M. Ahn, E. Martinez, G. S. D. Beach, Current-driven dynamics of chiral ferromagnetic domain walls. *Nat. Mater.* **12**, 611–616 (2013).

14. A. Manchon, J. Železný, I. M. Miron, T. Jungwirth, J. Sinova, A. Thiaville, K. Garello, P. Gambardella, Current-induced spin-orbit torques in ferromagnetic and antiferromagnetic systems. *Rev. Mod. Phys.* **91**, 035004 (2019).
15. E. B. Myers, D. C. Ralph, J. A. Katine, R. N. Louie, R. A. Buhrman, Current-induced switching of domains in magnetic multilayer devices. *Science* **285**, 867–870 (1999).
16. S. Murakami, N. Nagaosa, S. C. Zhang, Dissipationless quantum spin current at room temperature. *Science* **301**, 1348–1351 (2003).
17. N. Nagaosa, J. Sinova, S. Onoda, A. H. MacDonald, N. P. Ong, Anomalous hall effect. *Rev. Mod. Phys.* **82**, 1539–1592 (2010).
18. D. Pesin, A. H. MacDonald, Spintronics and pseudospintronics in graphene and topological insulators. *Nat. Mater.* **11**, 409–416 (2012).
19. A. A. Burkov, Weyl metals. *Annu. Rev. Condens. Matter Phys.* **9**, 359–378 (2018).
20. N. P. Armitage, E. J. Mele, A. Vishwanath, Weyl and Dirac semimetals in three-dimensional solids. *Rev. Mod. Phys.* **90**, 015001 (2018).
21. Y. Araki, J. Ieda, Intrinsic torques emerging from anomalous velocity in magnetic textures. *Phys. Rev. Lett.* **127**, 277205 (2021).
22. Z. Fang, N. Nagaosa, K. S. Takahashi, A. Asamitsu, R. Mathieu, T. Ogasawara, H. Yamada, M. Kawasaki, Y. Tokura, K. Terakura, The anomalous hall effect and magnetic monopoles in momentum space. *Science* **302**, 92–95 (2003).
23. S. Itoh, Y. Endoh, T. Yokoo, S. Ibuka, J.-G. Park, Y. Kaneko, K. S. Takahashi, Y. Tokura, N. Nagaosa, Weyl fermions and spin dynamics of metallic ferromagnet $SrRuO_3$. *Nat. Commun.* **7**, 11788 (2016).
24. K. Takiguchi, Y. K. Wakabayashi, H. Irie, Y. Krockenberger, T. Otsuka, H. Sawada, S. A. Nikolaev, H. Das, M. Tanaka, Y. Taniyasu, H. Yamamoto, Quantum transport evidence of Weyl fermions in an epitaxial ferromagnetic oxide. *Nat. Commun.* **11**, 4969 (2020).
25. J. Matsuno, N. Ogawa, K. Yasuda, F. Kagawa, W. Koshibae, N. Nagaosa, Y. Tokura, M. Kawasaki, Interface-driven topological Hall effect in $SrRuO_3$-$SrIrO_3$ bilayer. *Sci. Adv.* **2**, e1600304 (2016).
26. P. Zhang, A. Das, E. Barts, M. Azhar, L. Si, K. Held, M. Mostovoy, T. Banerjee, Robust skyrmion-bubble textures in $SrRuO_3$ thin films stabilized by magnetic anisotropy. *Phys. Rev. Res.* **2**, 032026 (2020).
27. M. Feigenson, J. W. Reiner, L. Klein, Efficient current-induced domain-wall displacement in $SrRuO_3$. *Phys. Rev. Lett.* **98**, 247204 (2007).
28. M. Yamanouchi, T. Oyamada, K. Sato, H. Ohta, J. Ieda, Current-induced modulation of coercive field in the ferromagnetic oxide $SrRuO_3$. *IEEE Trans. Mag.* **55**, 1400604 (2019).
29. D. C. Worledge, T. H. Geballe, Negative spin-polarization of $SrRuO_3$. *Phys. Rev. Lett.* **85**, 5182, 5185 (2000).
30. Y. Ou, Z. Wang, C. S. Chang, H. P. Nair, H. Paik, N. Reynolds, D. C. Ralph, D. A. Muller, D. G. Schlom, R. A. Buhrman, Exceptionally high, strongly temperature dependent, spin Hall conductivity of $SrRuO_3$. *Nano Lett.* **19**, 3663–3670 (2019).
31. I. M. Miron, G. Gaudin, S. Auffret, B. Rodmacq, A. Schuhl, S. Pizzini, J. Vogel, P. Gambardella, Current-driven spin torque induced by the Rashba effect in a ferromagnetic metal layer. *Nat. Mater.* **9**, 230–234 (2010).
32. D. Xiao, M.-C. Chang, Q. Niu, Berry phase effects on electronic properties. *Rev. Mod. Phys.* **82**, 1959–2007 (2010).
33. Q. Gan, R. A. Rao, C. B. Eom, L. Wu, F. Tsui, Lattice distortion and uniaxial magnetic anisotropy in single domain epitaxial (110) films of $SrRuO_3$. *J. Appl. Phys.* **85**, 5297–5299 (1999).
34. A. F. Marshall, L. Klein, J. S. Dodge, C. H. Ahn, J. W. Reiner, L. Mieville, L. Antagonazza, A. Kapitulnik, T. H. Geballe, M. R. Beasley, Lorentz transmission electron microscope study of ferromagnetic domain walls in $SrRuO_3$: Statics, dynamics, and crystal structure correlation. *J. Appl. Phys.* **85**, 4131–4140 (1999).
35. B. Nadgorny, M. S. Osofsky, D. J. Singh, G. T. Woods, R. J. Soulen Jr., M. K. Lee, S. D. Bu, C. B. Eom, Measurements of spin polarization of epitaxial $SrRuO_3$ thin films. *Appl. Phys. Lett.* **82**, 427–429 (2003).
36. R. Ilan, A. G. Grushin, D. I. Pikulin, Pseudo-electromagnetic fields in 3D topological semimetals. *Nat. Rev. Phys.* **2**, 29–41 (2020).
37. Y. Araki, Magnetic textures and dynamics in magnetic Weyl semimetals. *Ann. Phys.* **532**, 1900287 (2020).
38. J. M. Rondinelli, N. M. Caffrey, S. Sanvito, N. A. Spaldin, Electronic properties of bulk and thin film $SrRuO_3$: Search for the metal-insulator transition. *Phys. Rev. B* **78**, 155107 (2008).

Acknowledgments

Funding: This work was supported in part by the Japan Society for the Promotion of Science KAKENHI (grants nos. 20H02598, 20H02174, and 19H05622) and the Center for Spintronics Research Network. Y.A. is supported by the Leading Initiative for Excellent Young Researchers (LEADER). **Author contributions:** M.Y., J.I., and Y.A. designed this research project. M.Y. fabricated samples with advice from H.O. and carried out measurements of magnetotransport and of the effective magnetic-field acting on domain walls. T.S. carried out the magnetization measurements. Y.A. and J.I. developed the theory of topological Hall torque. M.Y., J.I., and Y.A. wrote the paper with input from T.U. All authors contributed to the discussion of this research. **Competing interests:** The authors declare that they have no competing interests. **Data and materials availability:** All data needed to evaluate the conclusions in the paper are present in the paper and/or the Supplementary Materials.

Submitted 25 July 2021
Accepted 25 February 2022
Published 15 April 2022
10.1126/sciadv.abl6192